The role of β_1 precipitates in the bio-corrosion performance of Mg–3Zn in simulated body fluid

Lu, Y.; Bradshaw, Andrew; Chiu, Yu-Lung; Jones, I.p.

DOI:
10.1016/j.jallcom.2014.06.078

License:
Other (please specify with Rights Statement)

Document Version
Peer reviewed version

Citation for published version (Harvard):
Lu, Y, Bradshaw, A, Chiu, Y-L & Jones, IP 2014, 'The role of β_1 precipitates in the bio-corrosion performance of Mg–3Zn in simulated body fluid', *Journal of Alloys and Compounds*, vol. 614, pp. 345-352. https://doi.org/10.1016/j.jallcom.2014.06.078

The role of β_1' precipitates in the bio-corrosion performance of Mg-3Zn in simulated body fluid

Y. Lu, A.R. Bradshaw, Y. L. Chiu, I.P. Jones

PII: S0925-8388(14)01423-6
DOI: http://dx.doi.org/10.1016/j.jallcom.2014.06.078
Reference: JALCOM 31494

To appear in: *Journal of Alloys and Compounds*

Received Date: 30 May 2014
Revised Date: 9 June 2014
Accepted Date: 10 June 2014

Please cite this article as: Y. Lu, A.R. Bradshaw, Y. L. Chiu, I.P. Jones, The role of β_1' precipitates in the bio-corrosion performance of Mg-3Zn in simulated body fluid, *Journal of Alloys and Compounds* (2014), doi: http://dx.doi.org/10.1016/j.jallcom.2014.06.078

The role of β_1' precipitates in the bio-corrosion performance of Mg-3Zn in simulated body fluid

Y. Lu *, A. R. Bradshaw, Y. L. Chiu, I. P. Jones

School of Metallurgy and Materials, University of Birmingham, Edgbaston, Birmingham, B15 2TT, United Kingdom

ABSTRACT

Mg-Zn alloys are promising candidate materials for medical applications. The bio-corrosion performance of Mg-3 wt% Zn has been studied at 37 ℃ in simulated body fluid (SBF) using immersion tests and electrochemical measurements. Heat treatments (solution treatment and ageing) were used to alter the microstructure and adjust the volume fraction of precipitates. It has been found that, in the solution treated sample, the dissolution of (α-Mg +MgZn) eutectic phases led to a low corrosion rate ($3.05 \pm 0.20\ mL/cm^2/day$). The volume fraction of precipitates increases with ageing time at 160 ℃ and causes the corrosion performance to deteriorate because of micro-cathodic effects. Thus the aged sample with the largest volume fraction of precipitates exhibits the worst corrosion resistance ($4.65 \pm 0.01\ mL/cm^2/day$).

Key words: Mg-Zn; bio-corrosion; microstructure; heat treatment

1. Introduction

Magnesium alloys are promising candidates for biomedical applications because they are light and possess an elastic modulus close to that of human bones, excellent biocompatibility and attractive biodegradability, as compared with many other structural metals. Magnesium is very reactive due to its electrochemical potential [1]. Magnesium shows a significant tendency for corrosion, especially in a Cl^- containing solution including human body fluid or blood plasma [2]. The following reaction summarizes the corrosion of magnesium:

$$Mg + 2H_2O \rightarrow Mg(OH)_2 + H_2 \uparrow \qquad (1)$$

Moreover, magnesium alloys are easily attacked by micro-galvanic corrosion [3, 4]. There is a correct level of biodegradability for every application. It is not desirable for the material to degrade completely before tissue healing has taken place.

It is well known that microstructure plays an important role in the corrosion performance of materials [5-8]. For instance, variation of the morphology, volume fraction and distribution of secondary phases can change the corrosion resistance [9, 10]. The influence of $Mg_{17}Al_{12}$ (β phase) on the corrosion behaviour of AZ91 alloys has been studied widely [2, 11]. The β phase can act as either a corrosion barrier or a galvanic cathode, depending on its amount and distribution. Fine and continuously distributed β phase retards the development of corrosion, while isolated coarse β phase causes micro-galvanic corrosion and accelerates the overall corrosion rate. These studies however mainly focus on micrometre scale secondary phases. Concerning the role of nano-scale secondary phases, insufficient results have been reported. Song [9] reported that solution-treated Mg-5Zn alloy has the best corrosion resistance and that aged alloy has the worst corrosion resistance because of copious Mg_xZn_y second phases some hundreds of nanometres across. Liang [12] found that the presence of base-centered orthorhombic β' precipitates after ageing results in the decreased corrosion resistance of Mg-7Gd-3Y-0.4Zr. Ageing decreases the corrosion resistance with increasing ageing time to 193 h, due to the formation of precipitates (β'' (DO_{19}), β' (cbco) and β_1 (fcc)) in Mg-10Gd-3Y-0.4Zr alloy [8]. Precipitates of different sizes may have different effects on the corrosion resistance of the alloy system. For instance, the small second phase with different types or precipitation sequences accelerates the corrosion as a galvanic cathode. However, the corrosion resistance of Mg-10Gd-3Y-0.4Zr alloy increases after a long time ageing (500 h), because the large precipitates formed in a type of continuous network acted as corrosion barriers [8]. There is however no clear relationship identified between bio-corrosion resistance and

microstructure of Mg-Zn alloys. There is therefore a need to investigate the effect of very fine precipitates on bio-corrosion performance. Heat treatment is an effective way to change the volume fraction of precipitates and therefore to alter the corrosion rate. The influence of ageing and precipitation on the bio-corrosion behaviour of Mg-Zn alloys is not well studied. This study is aimed at understanding the effect of very fine secondary phases on the bio-corrosion behaviour of Mg-3Zn alloys.

Various chemical elements such Al, Ca, Zn, Mn and the rare earths are used in magnesium biomaterials. Although the Al and rare earth containing magnesium alloy provide relatively high strength and good corrosion resistance, the toxicity of these elements needs to be considered. It has been reported that Al is harmful to osteoblasts and to neuron function [13]. Its accumulation can cause muscle fibre damage and decreases osteoblast viability [14, 15]. Some rare earth elements such as Pr, Ce and Lu are toxic to the human body [16]. A high concentration of Y can change the expression of some rat genes and have adverse effects on DNA transcription factors [17]. Excessive Mn may induce neurotoxicity [18]. Ca is a bio-friendly element, but the alloy becomes brittle with increasing addition of Ca. In this study, Zn (kept at 3 wt%) has been chosen as the alloying element because: 1) zinc is a biologically benign element; 2) zinc has a good strengthening effect in magnesium; 3) zinc is beneficial in increasing the tolerance limits of impurities [19, 20]; 4) zinc can improve castability (although a high zinc content may cause hot-cracking and microporosity during solidification). Mg-Zn based alloys have a remarkable age hardening response. There are five intermetallic phases between magnesium and znic, viz. Mg_7Zn_3, MgZn, Mg_2Zn_3, $MgZn_2$ and Mg_2Zn_{11} [21]. During the ageing of a solution alloy, precipitation occurs according to the following sequence [22-27]:

$$SSSS \rightarrow Guinier\ Preston\ (GP) zones \rightarrow \beta_1' \rightarrow \beta_2' \rightarrow \beta\ (MgZn)$$

β_1' typically has a rod (sometimes a blocky) morphology with its longitudinal direction along [0001] of the matrix. β_1' has a base-centred monoclinic structure (a=2.596 nm,

b=1.428 nm, c=0.514 nm, γ=102.5°) [28]. β_2' appears as coarse plates parallel to the basal plane of the matrix or occasionally as laths perpendicular to the basal plane. β_2' has a hexagonal structure (a=0.523 nm, c=0.858 nm) [28, 29]. The structure of the equilibrium MgZn (β) phase is rhombohedral with a=2.569 nm and c=1.8104 nm [30].

2. Materials and Methods

2.1 Materials

Magnesium ingots were prepared by melting magnesium (99.95 wt%) and zinc (99.99 wt%) in a vacuum induction furnace backfilled with a protective atmosphere of high purity argon gas. The composition of the material (nominally Mg - 3 wt% Zn) was determined using a Rigaku NEX-CG XRF system as (wt%): Zn - 3.08 $\pm$ 0.03, Si - < 0.0001, Fe - 0.0045, Cu - < 0.0001, Ni - 0.0006, Mg - balance. The as-cast ingot was solution treated at 310 ℃ for 24 h followed by water quenching. Subsequently ageing was performed at 160 ℃ in air for 10 h, 25 h, 50 h, 96 h and 144 h, followed by water quenching.

2.2 Microstructural characterization

Samples for metallography were mechanically polished down to 0.25 μm diamond compound and then etched in a solution containing 50 ml distilled water, 150 ml ethanol and 1 ml acetic acid. The microstructure was observed using an optical microscope (Zeiss Axioskop 2) and scanning electron microscopes (Philips XL30 and JEOL JSM-7000F). Image J was used to analyse the grain size. At least 20 measurements of grain size were made at a magnification of 100×.

2.3 Quantitative analysis

Quantitative stereology was used to measure the volume fraction of precipitates in the thin metal foil. After truncation and overlap corrections, the volume fraction of fine precipitates (f_v) was determined using the equation below [31-33]:

$$f_v = -\ln(1 - A_A)\left(\frac{DL}{DL+(\frac{D}{2}+L)t}\right) \qquad (2)$$

where D is the diameter of the rod-shaped precipitates, L is the length of the precipitates, t is the specimen thickness and A_A is the projected area fraction of the precipitates.

A transmission electron microscope (JEOL-2100HT TEM) was used to study the fine precipitates. In order to measure the dimensions of the rod-like precipitates, they were observed along <0001> and $< 2\bar{1}\bar{1}0 >$ matrix zone axes. Bright field images taken at magnifications of 8kx and 10kx were used to measure the projected area fraction of precipitates using Image J. The reported data represent an average of at least 300 measurements for each condition.

2.3 Immersion Test

The degradation rate was determined by measuring the hydrogen evolution rate when the samples were immersed in Kokubo's simulated body fluid (SBF) at 37 ℃ for up to 10 days [34]. To minimize any variations in the immersion environment, the SBF solution was refreshed every 24 h and the ratio of sample surface to volume of SBF maintained at 1 cm^2 : 100 mL. The samples (10 mm × 10 mm × 2 mm) were polished down to 1 μm before the immersion test. Three measurements were carried out for each condition. After immersion, the specimens were taken out, rinsed gently in the de-ionised water and dried with cool air. A solution of 180 g/L CrO_3 was used to clean carefully the tested samples to remove the corrosion products with minimal damage to the sample.

2.4 Electrochemical Measurements

The electrochemical stability of the alloy was measured using an electrochemical station (ACM INSTRUMENT Gill AC). Samples with 1 cm^2 exposed area were polished to 1 μm before the test and tested in 100 mL SBF solution at 37 ℃. The open circuit potential (OCP) was recorded with an immersion time of up to 60 minutes. The

potentiodynamic tests were then started at a fixed value (50 mV above the OCP) and scanned at 1 mV/s until reaching about -500 mV relative to OCP. Three tests were performed for each sample condition to ensure reproducibility.

3. Results

3.1 Microstructure and bio-corrosion behaviour of the as-cast and the solution-treated alloys

Optical images of as-cast and solution-treated alloy are shown in Figure 1. After exposure at 310 ℃ for 24 h, the grains of alloy grow from 141 ± 8 μm to 232 ± 12 μm and the dendrite structure disappeared. The morphology of the as-cast alloy is presented in Figure 2. Spherical particles are distributed mainly within the grains, as shown in Figure 2(a). A close-up view (Figure 2(b)) shows eutectic morphology within the particle. The microstructure changes noticeably upon solution-treatment. After exposure at 310 ℃ for 24 h, the spherical products have largely been dissolved. The spherical particles are α-Mg + MgZn. The MgZn phase was identified using a crystallographic tilting experiment and EDX analysis (Figure 2). The EDX spectrum recorded from the dark region of the particle shows significant Mg and Zn peaks. The composition of the MgZn phase was 49.0 ± 3.7 at% Mg and 51.0 ± 3.7 at% Zn. The crystal structure was confirmed to be rhombohedral (a=2.6 nm and c=1.8 nm) from the electron diffraction patterns (Figure 2 (c)).

Figure 4 presents that the surface morphologies of the as-cast and solution-treated alloys. To the naked eye, the as-cast alloy suffers more obvious corrosion attack than the solution-treated alloy, as indicated by the significant dissolution of the sample. The bio-corrosion rates of the as-cast and solution-treated samples immersed in SBF at 37 ℃ for 10 days are 3.50 ± 0.20 mL/cm^2/day and 3.05 ± 0.20 mL/cm^2/day, respectively. The corrosion resistance is thus improved by the solution treatment. Figure 5 shows the surface morphology of the samples after immersion in SBF for 10 days. It can be seen that the corrosion of the as-cast sample is more severe than that of the solution-treated sample. Both the as-cast and solution-treated alloys suffer obvious

localised corrosion (pitting) as indicated by the arrows. As shown in the insert in Figure 5(a), severe dissolution of the magnesium matrix surrounding the (α- Mg + MgZn) phases occurred.

3.2 Microstructure and bio-corrosion of aged samples

3.2.1 Precipitate types

Figure 6 shows transmission electron micrographs from samples aged for 10 h, 25 h, 50 h, 96 h and 144 h at 160 ℃. It can clearly be seen that the rod-shaped precipitates are the most common type. As shown in Figures 6(a-b), only a small number of precipitates have formed at 160 ℃ after 10 h. The majority of the precipitates have a near circular cross section when viewed along [0001]. Furthermore, it can be seen that the long axis of the precipitates is parallel to [0001]. This is consistent with the β_1' precipitates described in the literature [28, 35, 36]. In the 25 h aged sample (Figures 6(c-d)) the density of the rod precipitates becomes higher. The length and density of the precipitates both increase with ageing time. After 50 h ageing, there are a few β_2' precipitates [29] which are end-on when viewed along $[2\bar{1}\bar{1}0]$, as indicated by arrows in the inset to Figure 6(e). The number density of the precipitates increases with the ageing time. Figure 6(j) shows that some precipitates have become obviously thicker after 144 h ageing.

3.2.2 Volume fraction of the fine precipitates

As illustrated in Figure 7, with increasing ageing time the average volume fraction of precipitates increases from 0.04 $\pm$ 0.02 % in the 10 h aged alloy to 3.03 $\pm$ 0.17 % in the 144 h aged alloy.

3.2.3 Bio-corrosion of aged samples

The variation of degradation rate with ageing time is presented in Figure 8. The bio-corrosion rate increases monotonically with ageing time. Figure 9 shows the surface morphology of the aged samples after exposure in SBF for 10 days. The

surfaces are decorated with pits (as indicated by the arrows). Occasional shallow corrosion pits can be observed in the 10 h aged sample, while serious corrosion occurs all over the surfaces of the other samples. With prolonged aging time, the corrosion morphology becomes more faceted as indicated by the double arrows, especially in the samples aged for 50 h, 96 h and 144 h, as shown in Figures 9(c-e). The rod shaped precipitates grow along [0001]. They show different orientations in different grains and this results in differently orientated corrosion morphologies (see Figure 9(f)). The proposed corrosion mechanism in the aged alloy is shown schematically in Figure 9(g). When the samples are immersed in SBF, micro-galvanic corrosion cells form between the fine precipitates and the magnesium matrix; hence, the magnesium matrix dissolves and the fine precipitates are undermined and fall from the surface which then forms these parallel filament-like trenches with different orientations in different grains.

3.3 Electrochemical tests

Figure 10 shows the open circuit potential (E_{ocp}) - time curves recorded during immersion in SBF for 3600 s. As can be seen in Figure 10, there is a tendency for the potential to fluctuate: the potential of the samples gradually shifts in the nobler direction during the test and at the end of immersion tends to become constant. The open circuit potential of the solution treated sample is obviously more positive than that of the other samples. Furthermore, E_{ocp} shifts towards more negative values with increasing ageing time.

The polarization curves are illustrated in Figure 11. Solution treatment gives rise to a shift in the polarization curve to a more positive potential and a lower cathodic current density. The improvement in the E_{corr} of the solution-treated sample can be attributed to the dissolution of the (α-Mg +MgZn) eutectic phases, thus reducing the susceptibility to galvanic corrosion. E_{corr} of aged samples decreases with ageing time, from -1732.0 mV at 160 ℃/10 h to -1837.2 mV at 160 ℃/144 h. The cathodic current density of the aged samples tends to increase with ageing time: thus the sample after 144 h ageing has the highest cathodic current density. The ageing sample with 50 h shows a similar E_{ocp}

and cathodic current density to the as-cast sample (as shown in Figure 10 and Figure 11). This is because the size and density of the fine precipitates (β_1') increase largely at 160 ℃/50 h and these plenty of fine precipitates cause more micro-galvanic couples, while the micrometer scale spherical particles (α-Mg + MgZn) are distributed in the as-cast sample and also act as effective cathodes. Both of precipitates deteriorate the corrosion resistance. Generally, the cathodic polarization curve represents the hydrogen evolution. The influence of heat treatment on the cathodic hydrogen evolution is clear.

3.4 Hardness

Upon ageing, the hardness increases as compared with that of the as-cast sample (48.8 $\pm$ 1.8 HV) and the solution-treated sample (52.9 $\pm$ 2.3 HV). The hardnesses of the aged alloys are shown in Figure 12. An age-hardening behaviour can be seen. The hardness peaks at 96 h (66.5 $\pm$ 3.2 HV) and then decreases.

4. Discussion

The degradation rate of the alloys is associated with the microstructure. In the as-cast sample, spherical eutectic nodules (α-Mg + MgZn) are dispersed with an average size of 5 μm. After solution treatment (310 ℃/ 24 h) the second phase dissolves. The corrosion resistance of the solution-treated sample is higher than that of the as-cast sample. This is because micro-galvanic coupling has built up between the secondary phase and the matrix; the eutectic MgZn acts as a cathode and the surrounding magnesium matrix as anode. The dissolution of the eutectic product upon solution treatment is evidently beneficial to the corrosion resistance. Song [9], Peng [8], Aung [37] and Liang [12] have reported a similar corrosion behaviour: the solution treatment improves the corrosion resistance of magnesium alloys, which is attributed to the absence of a second phase. Lunder [38] and Zhao [11] found the opposite behaviour for the corrosion of AZ91 alloy. This is because in that case a large amount of β phase ($Mg_{17}Al_{12}$) had formed an interconnected network throughout the microstructure which acted as a corrosion barrier rather than a cathode. In the current study, however,

spherical regions with a low volume fraction are distributed randomly and cannot act as a corrosion barrier. The micro-galvanic corrosion is initiated in the magnesium matrix adjacent to the sphere. As shown in the inset to Figure 5(a), the surrounding magnesium matrix is corroded and thus leaves a narrow and black trench around the sphere.

Subsequently, upon ageing, fine precipitates form and the quantity increases with increasing ageing time (as indicated in Figure 7). The degradation rate of the aged samples is sensitive to the volume fraction of fine precipitates. In Figure 13 the linear regression suggests that as the precipitate volume fraction increases the degradation rate increases. This is again attributed to micro-galvanic couples between the fine precipitates and the matrix. The fine precipitates are nobler than the magnesium matrix. Therefore, the fine precipitates act as micro-cathodes while the surrounding matrix acts as the anode. The effect of fine precipitates on the hardness and bio-corrosion rate of the alloy is evident (Figures 12 and 13). The decomposition of the supersaturated solid solution of Zn in Mg produces age hardening. The age hardening response of alloy at 160 ℃ is illustrated in Figure 12. Ageing increases the peak hardness by 28 %. The maximum increment in hardness is similar with the value reported in the literature [26, 35, 39]: 23 % in Mg-9 wt% Zn, 25 % in Mg-2.8 at% Zn and 31 % in Mg-2.4 at% Zn, respectively. The age hardening involves two precipitates: rods (β_1') and coarse plates β_2' [36]. The rod-like β_1' precipitates are primarily responsible for the age-hardening. The hardness peaks at 96 h because of the dense dispersion of rod-shaped β_1'. After ageing for 144 h, the hardness decreases due to the transformation of β_1' to disc-shaped β_2' [35]. β_2' precipitates are easily bypassed by dislocations and provide less obstruction to their movement [35]. As such, an application tailored ageing time is needed to achieve an appropriate performance (strength (hardness) and bio-corrosion).

5. Conclusions

Heat treatment is an effective way to alter the bio-corrosion rate of Mg-3Zn in SBF. The corrosion resistance of the solution-treated sample is better than that of the as-cast and

of the aged samples. The absence of eutectic (α-Mg + MgZn) phases reduces micro-galvanic corrosion. Nano-scale precipitates formed during ageing decrease the corrosion resistance. The increase in bio-corrosion rate with ageing time appears to be monotonic. With increasing ageing time, Mg alloys display worse corrosion resistance because of the precipitates (β_1'). The corrosion morphology consists of parallel filament-like trenches which mirror the growth direction of the β_1' precipitates in the aged alloys. Moreover, the hardness peaks after 96 hours ageing at 160 ℃ because of dense dispersion of rod-shaped β_1'. The size, distribution and volume fraction of precipitates are important parameters that should be considered in order to tailor the microstructure and performance of magnesium alloys for different bio-medical applications.

Acknowledgement

Y. Lu is grateful for financial support from the University of Birmingham and a scholarship awarded by the China Scholarship Council.

References

[1] R.W. Revie and H.H. Uhlig, *Corrosion and corrosion control (Fourth edition),* 2008, Hoboken, New Jersey: John Wiley & Sons. p. 399.

[2] G.L. Song and A. Atrens, *Corrosion mechanisms of magnesium alloys.* Advanced Engineering Materials, 1999. **1**(1): p. 11-33.

[3] G.L. Song and A. Atrens, *Understanding magnesium corrosion - A framework for improved alloy performance.* Advanced Engineering Materials, 2003. **5**(12): p. 837-858.

[4] G.L. Song, A. Atrens, and M. Dargusch, *Influence of microstructure on the corrosion of diecast AZ91D.* Corrosion Science, 1999. **41**(2): p. 249-273.

[5] E.L. Zhang, L. Yang, J.W. Xu, and H.Y. Chen, *Microstructure, mechanical properties and bio-corrosion properties of Mg-Si(-Ca, Zn) alloy for biomedical application.* Acta Biomaterialia, 2010. **6**(5): p. 1756-1762.

[6] K.D. Ralston, N. Birbilis, and C.H.J. Davies, *Revealing the relationship between grain size and corrosion rate of metals.* Scripta Materialia, 2010. **63**(12): p. 1201-1204.

[7] M. Liu, D. Qiu, M.C. Zhao, G. Song, and A. Atrens, *The effect of crystallographic orientation on the active corrosion of pure magnesium.* Scripta Materialia, 2008. **58**(5): p. 421-424.

[8] L.M. Peng, J.W. Chang, X.W. Guo, A. Atrens, W.J. Ding, and Y.H. Peng, *Influence of heat treatment and microstructure on the corrosion of magnesium alloy Mg-10Gd-3Y-0.4Zr.* Journal of Applied Electrochemistry, 2009. **39**(6): p. 913-920.

[9] Y.W. Song, E.H. Han, D.Y. Shan, C.D. Yim, and B.S. You, *The role of second phases in the*

corrosion behavior of Mg-5Zn alloy. Corrosion Science, 2012. **60**: p. 238-245.

[10] H.R. Bakhsheshi-Rad, M.R. Abdul-Kadir, M.H. Idris, and S. Farahany, *Relationship between the corrosion behavior and the thermal characteristics and microstructure of Mg-0.5Ca-xZn alloys.* Corrosion Science, 2012. **64**: p. 184-197.

[11] M.C. Zhao, M. Liu, G.L. Song, and A. Atrens, *Influence of the beta-phase morphology on the corrosion of the Mg alloy AZ91.* Corrosion Science, 2008. **50**(7): p. 1939-1953.

[12] S.Q. Liang, D.K. Guan, and X.P. Tan, *The relation between heat treatment and corrosion behavior of Mg-Gd-Y-Zr alloy.* Materials & Design, 2011. **32**(3): p. 1194-1199.

[13] C.H. Ku, D.P. Piolettli, M. Browne, and P.J. Gregson, *Effect of different Ti-6A1-4V surface treatments on osteoblasts behaviour.* Biomaterials, 2002. **23**(6): p. 1447-1454.

[14] M. Shingde, J. Hughes, R. Boadle, E.J. Wills, and R. Pamphlett, *Macrophagic myofasciitis associated with vaccine-derived aluminium.* Medical Journal of Australia, 2005. **183**(3): p. 145-146.

[15] S.S. Abd El-Rahman, *Neuropathology of aluminum toxicity in rats (glutamate and GABA impairment).* Pharmacological Research, 2003. **47**(3): p. 189-194.

[16] F. Witte, V. Kaese, H. Haferkamp, E. Switzer, A. Meyer-Lindenberg, C.J. Wirth, and H. Windhagen, *In vivo corrosion of four magnesium alloys and the associated bone response.* Biomaterials, 2005. **26**(17): p. 3557-3563.

[17] W.D. Yang, P. Zhang, J.S. Liu, and Y.F. Xue, *Effect of long-term intake of Y3+ in drinking water on gene expression in brains of rats.* Journal of Rare Earths, 2006. **24**(3): p. 369-373.

[18] N.A. Bock, F.F. Paiva, G.C. Nascimento, J.D. Newman, and A.C. Silva, *Cerebrospinal fluid to brain transport of manganese in a non-human primate revealed by MRI.* Brain Research, 2008. **1198**: p. 160-170.

[19] W.S. Loose, *Corrosion and Protection of Magnesium*, ed. L.M. Pidgeon, J.C. Mathes, and N.E. Woldmen1946: ASM International, Materials Park. p.173-260.

[20] M.M. Avedesian and H. Baker, *ASM Specialty Handbook: Magnesium and magnesium alloys,* 1999: ASM international. p.17.

[21] J.B. Clark and F.N. Rhines, *Central region of the Mg-Zn phase diagram.* Transactions of the American Institute of Mining and Metallurgical Engineers, 1957. **209**: p. 425-430.

[22] L. Sturkey and J.B. Clark, *Mechanism of age-hardening in magnesium zinc alloys.* Journal of the Institute of Metals, 1959. **88**(4): p. 177-181.

[23] J.B. Clark, *Transmission electron microscopy study of age hardening in a Mg-5 wt% Zn alloy.* Acta Metallurgica, 1965. **13**(12): p. 1281-1289.

[24] M. Bernole, J. Gallot, and R. Graf, *Electron micrography of Mg-6% Zn alloy using electrolytic thinning.* Journal of Microscopy, 1965. **4**: p. 787-792.

[25] G. Mima and Y. Tanaka, *The main factors affecting the aging of magnesium-zinc alloys.* Transactions of Journal of Japan Institute of Metals and Materials (JIM), 1971. **12**: p. 76-81.

[26] J. Buha, *Reduced temperature (22-100 degrees C) ageing of an Mg-Zn alloy.* Materials Science and Engineering A - Structural Materials Properties Microstructure and Processing, 2008. **492**(1-2): p. 11-19.

[27] J.F. Nie, *Precipitation and hardening in magnesium alloys.* Metallurgical and Materials Transactions A - Physical Metallurgy and Materials Science, 2012. **43A**(11): p.

3891-3939.

[28] X. Gao and J.F. Nie, *Characterization of strengthening precipitate phases in a Mg-Zn alloy.* Scripta Materialia, 2007. **56**(8): p. 645-648.

[29] Y. Komura and K. Tokunaga, *Structural studies of stacking variants in Mg-base Friauf-Laves phases.* Acta Crystallographica Section B - Structural Science, 1980. **36**(Jul): p. 1548-1554.

[30] Y. Khan, *Dynamic temperature crystallization behavior of amorphous and liquid Mg70Zn30 alloy.* Journal of Materials Science, 1989. **24**(3): p. 963-973.

[31] J. Jain, P. Cizek, W.J. Poole, and M.R. Barnett, *Precipitate characteristics and their effect on the prismatic-slip-dominated deformation behaviour of an Mg-6 Zn alloy.* Acta Materialia, 2013. **61**(11): p. 4091-4102.

[32] E.E. Underwood, *Stereology, or the quantitative evaluation of microstructures.* Journal of Microscopy, 1969. **89**: p. 161-180.

[33] G.E. Pellissier, *Stereology and quantitative metallography,* 1972, Atlantic City: American Society for Testing and Materials.

[34] T. Kokubo and H. Takadama, *How useful is SBF in predicting in vivo bone bioactivity?* Biomaterials, 2006. **27**(15): p. 2907-2915.

[35] L.Y. Wei, G.L. Dunlop, and H. Westengen, *Precipitation hardening of Mg-Zn and Mg-Zn-Re alloys.* Metallurgical and Materials Transactions A - Physical Metallurgy and Materials Science, 1995. **26**(7): p. 1705-1716.

[36] J.S. Chun and J.G. Byrne, *Precipitate strengthening mechanisms in magnesium zinc alloy single crystals.* Journal of Materials Science, 1969. **4**(10): p. 861-872.

[37] N.N. Aung and W. Zhou, *Effect of heat treatment on corrosion and electrochemical behaviour of AZ91D magnesium alloy.* Journal of Applied Electrochemistry, 2002. **32**(12): p. 1397-1401.

[38] O. Lunder, J.E. Lein, T.K. Aune, and K. Nisancioglu, *The role of Mg17Al12 phase in the corrosion of Mg alloy AZ91.* Corrosion, 1989. **45**(9): p. 741-748.

[39] C.L. Mendis, K. Oh-ishi, and K. Hono, *Enhanced age hardening in a Mg-2.4 at.% Zn alloy by trace additions of Ag and Ca.* Scripta Materialia, 2007. **57**(6): p. 485-488.

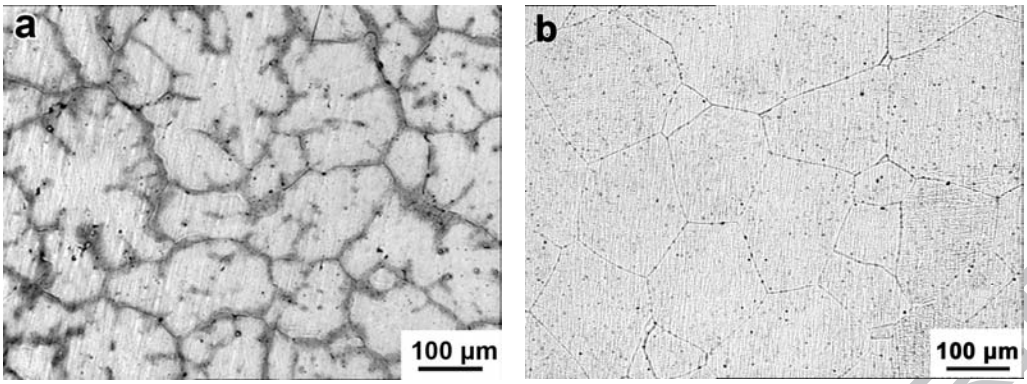

Figure 1 Optical microstructures: (a) as-cast MZ3; (b) after solution treatment (310 ℃/24 h). The grain size increases and dendrite structure disappears after the solution treatment.

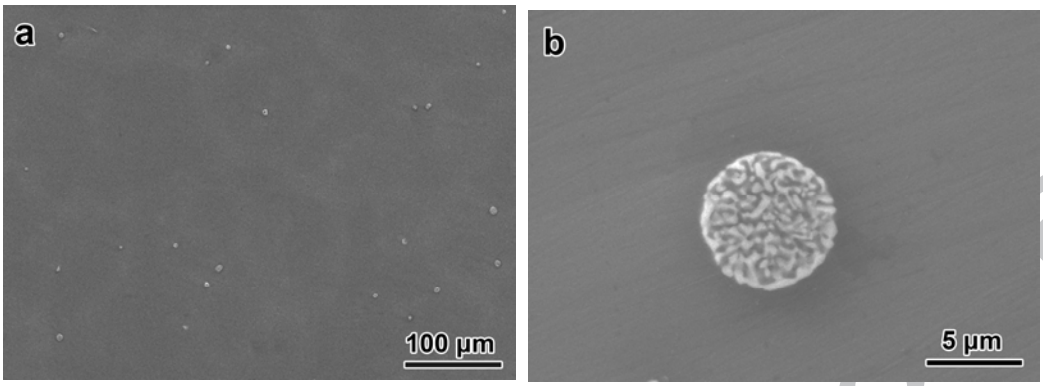

Figure 2 SEM micrographs showing the microstructure of the as-cast alloy (a) and a closer view of a spherical particle with typical eutectic product characteristics (b).

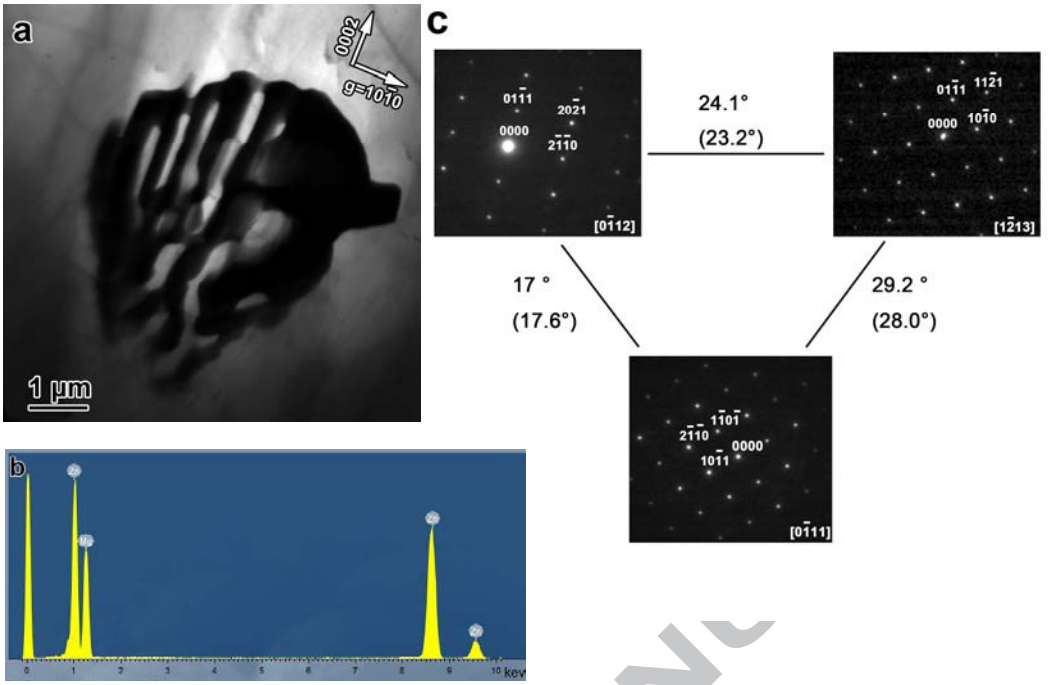

Figure 3 (a) TEM BF image showing the morphology of a particle in the as-cast alloy, the electron beam direction is close to [1$\bar{2}$10]; (b) EDX spectrum obtained from the dark region of the particle; (c) Electron diffraction patterns obtained from a crystallographic tilting experiment confirming the rhomobohedral structure. (The values without brackets are calculated values and the actual tilt angles are shown in brackets).

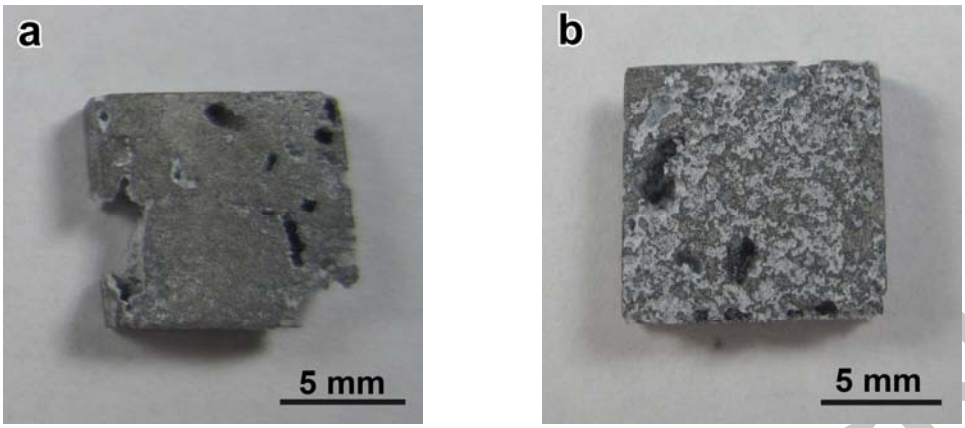

Figure 4 Photographs of immersed samples after 10 days in SBF at 37 ℃: (a) as-cast; (b) solution-treated. The partly dissolution of immersed samples can be observed, as illustrated by the cavities.

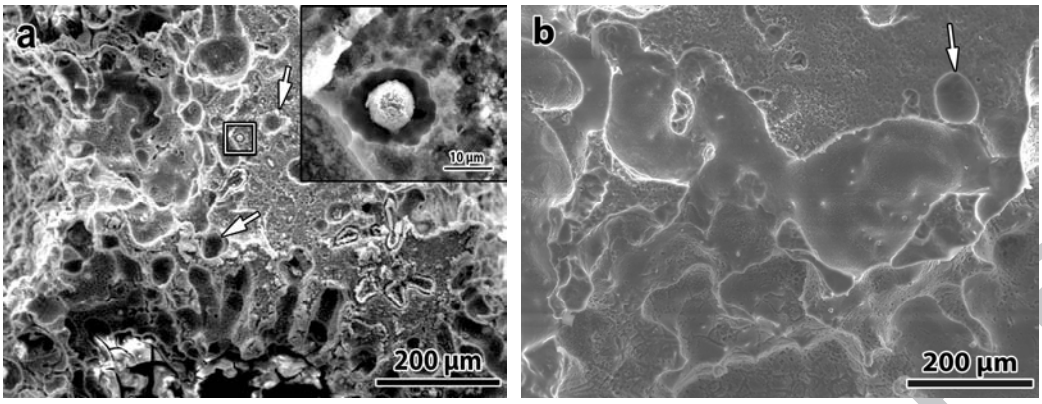

Figure 5 Surface morphologies of the as-cast alloy (a) and the solution-treated alloy (b) after 10 days' immersion in SBF (after removal of corrosion products). The inset is a closer view of the area highlighted in the white square showing the severe dissolution of the material surrounding a spherical particle. Corrosion pits are indicated by arrows.

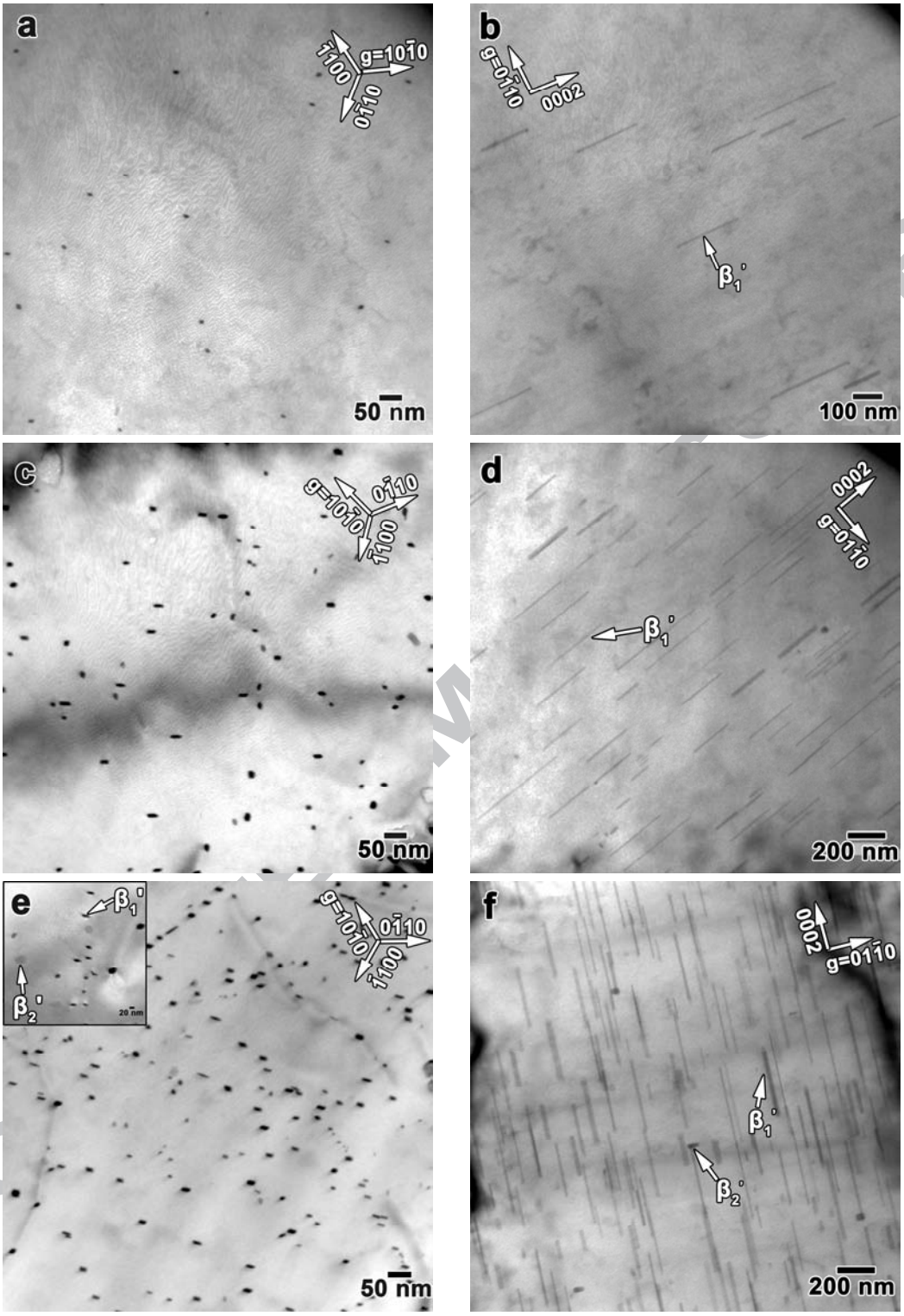
a
g=10$\bar{1}$0
$\bar{1}$100
01$\bar{1}$0
50 nm
b
g=0$\bar{1}$10
0002
β1'
100 nm
C
g=10$\bar{1}$0
01$\bar{1}$0
$\bar{1}$100
50 nm
d
0002
g=0$\bar{1}$10
β1'
200 nm
e
β1'
β2'
20 nm
g=10$\bar{1}$0
01$\bar{1}$0
$\bar{1}$100
50 nm
f
0002
g=01$\bar{1}$0
β1'
β2'
200 nm

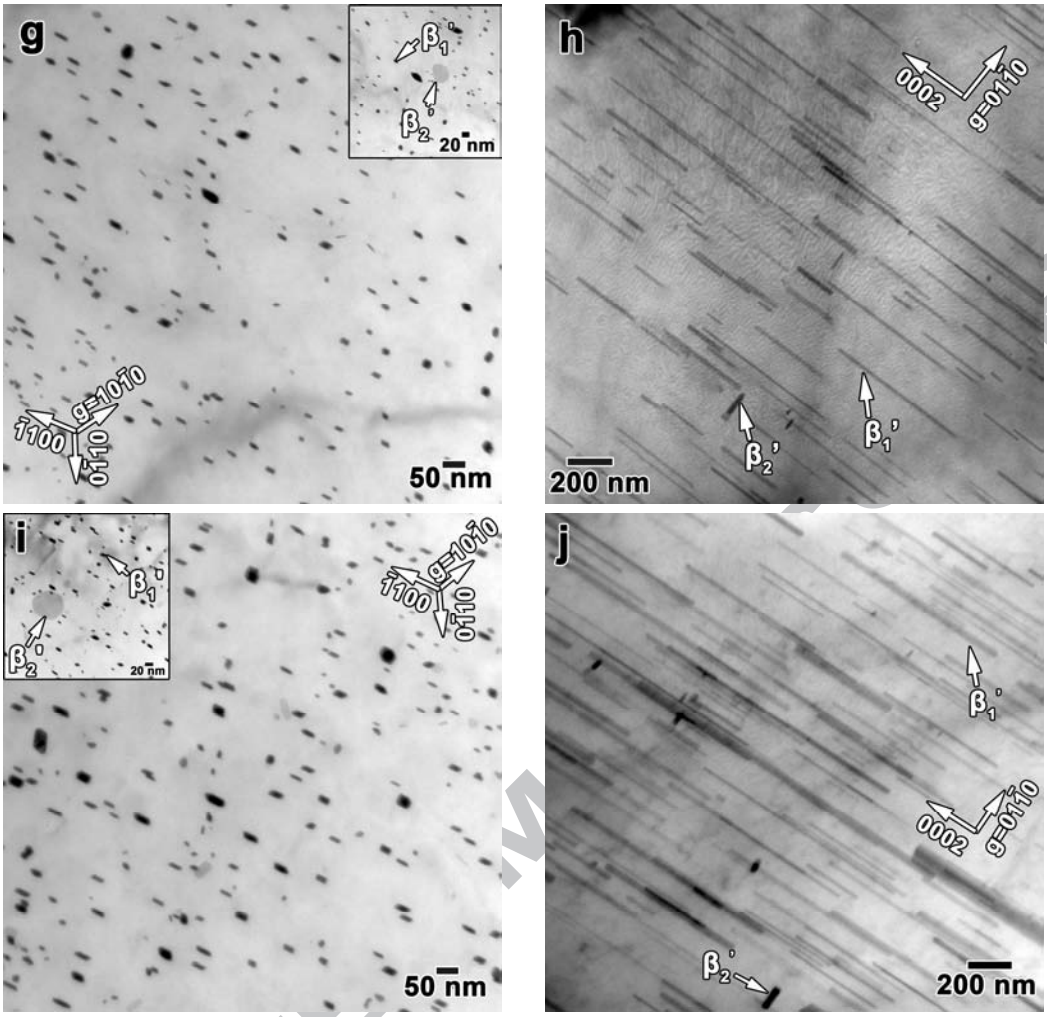

Figure 6 TEM micrographs showing precipitates in the samples aged at 160 ℃ for various times: (a-b) 10 h, (c-d) 25 h, (e-f) 50 h, (g-h) 96 h, (i-j) 144 h. For (a), (c) (e), (g) and (i), the electron beam direction was close to $[0001]$. For (b), (d), (f), (h) and (j) the electron beam direction was close to $[2\bar{1}\bar{1}0]$. More precipitates form with increasing ageing time.

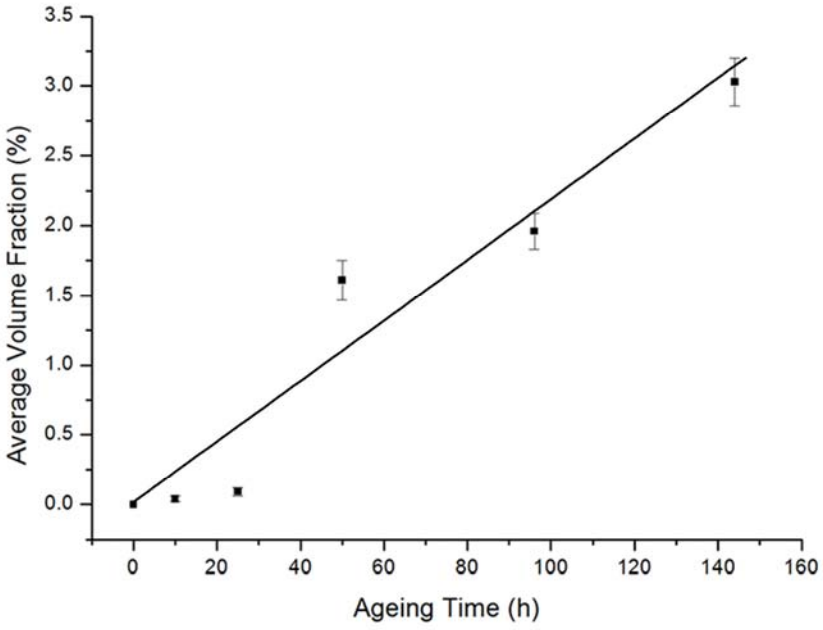

Figure 7 The volume fraction of rod-shaped precipitate volume fraction versus ageing time at 160 ℃. With increasing ageing time the volume fraction of precipitates increase.

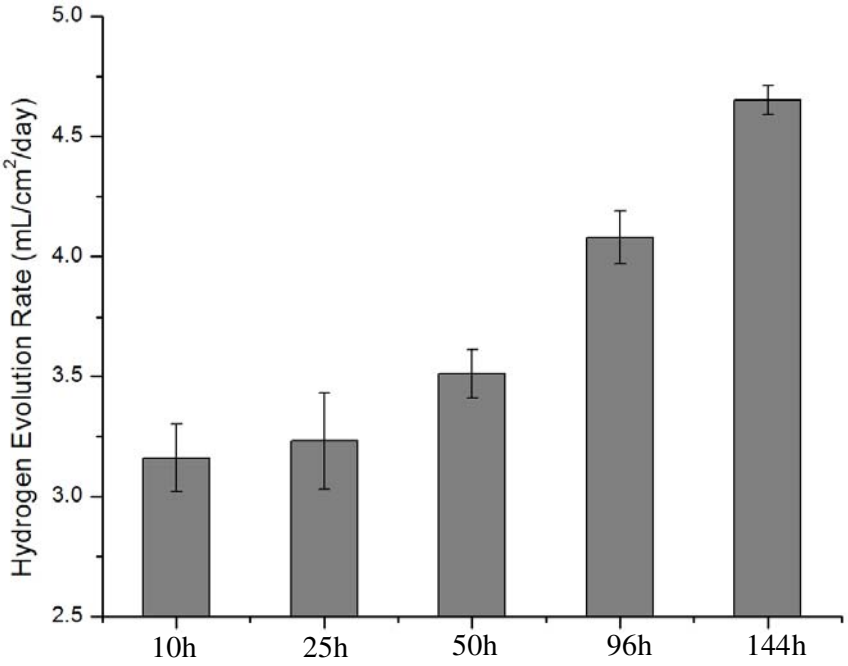

Figure 8 Degradation rate plotted against ageing time at 160 ℃. The degradation rate was measured using immersion in SBF for 10 days at 37 ℃. With ageing time the bio-corrosion rate increases monotonically.

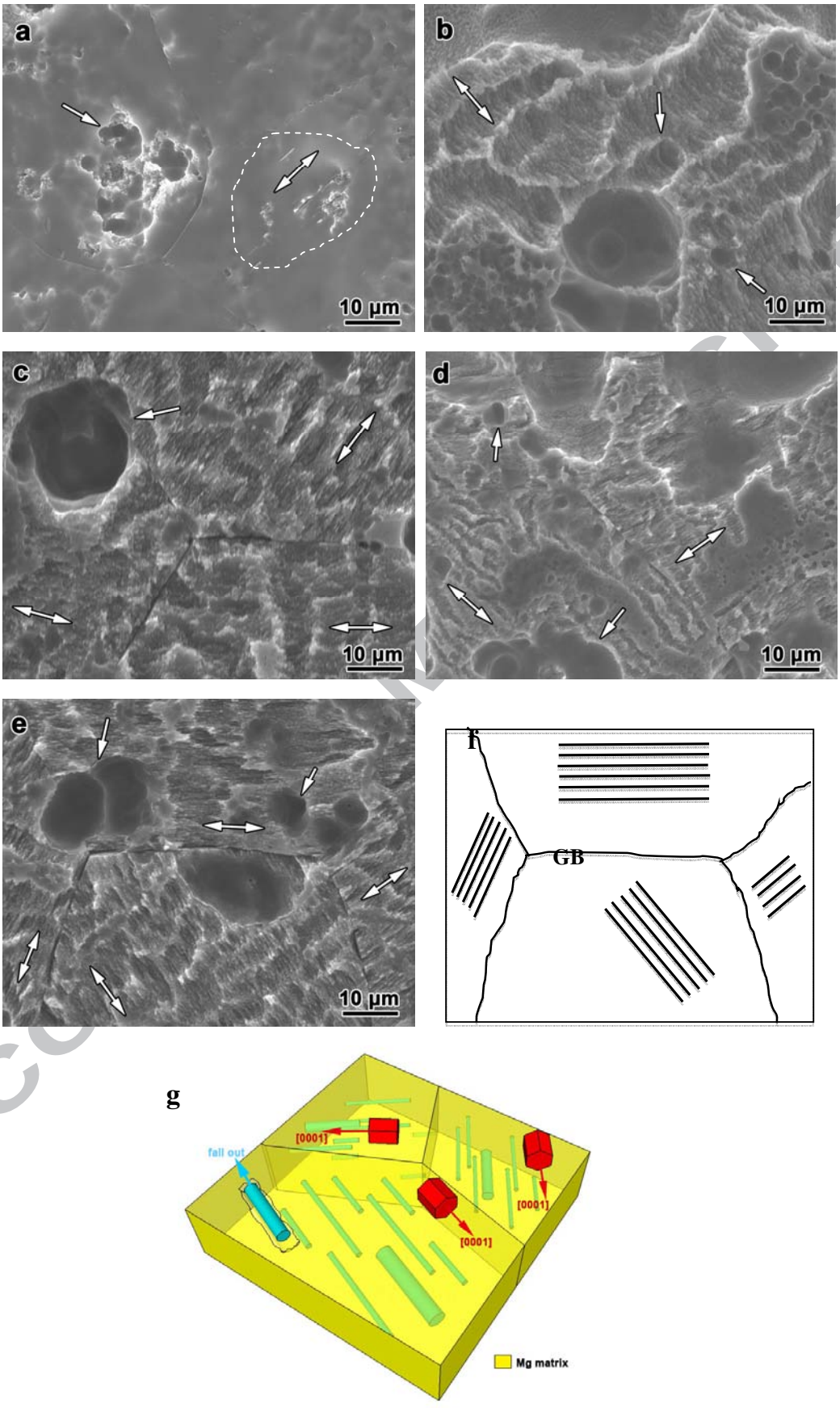
a
10 μm
b
10 μm
c
10 μm
d
10 μm
e
10 μm
f
GB
g
fall out
[0001]
[0001]
[0001]
Mg matrix

Figure 9 SEM micrographs showing the surface morphology after immersion in SBF for 10 days at 37 ℃ of samples aged for (a) 10 h; (b) 25 h; (c) 50 h; (d) 96h and (e) 144 h. Figure 7(f) is a schematic drawing of Figure 7(e). Figure 7(g) is another schematic drawing showing the precipitates and the observed corrosion morphology in the aged alloy. A hexagon is included in each grain to indicate the crystallographic orientation and rods are used to represent the fine precipitates.

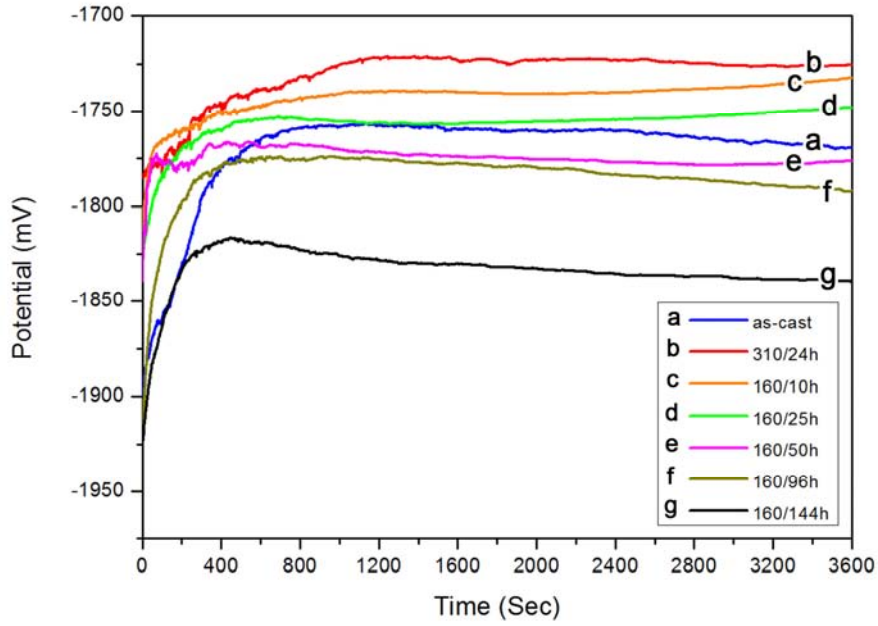

Figure 10 The open circuit potential measured from the samples in SBF at 37 ℃. The open circuit potential decreases with increasing ageing time.

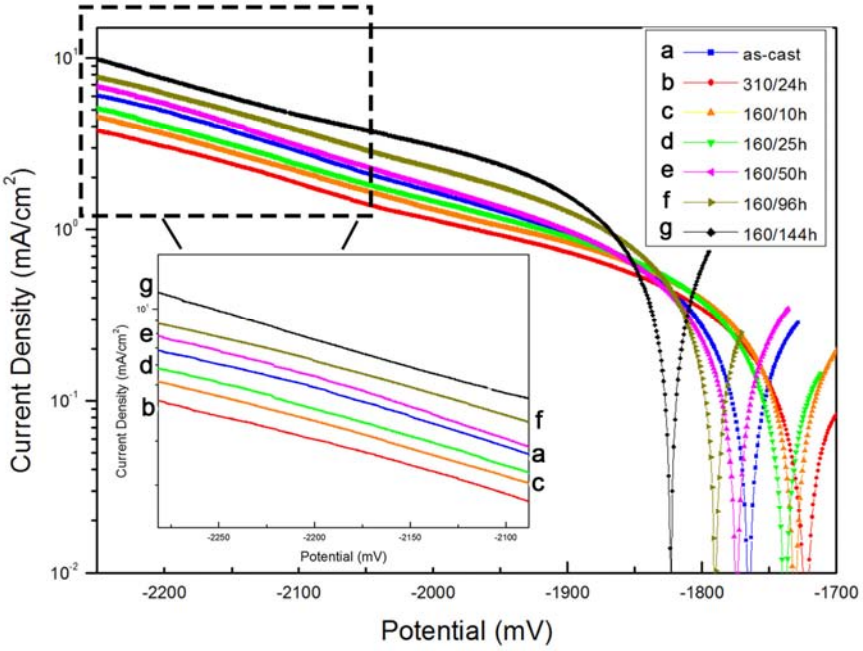

Figure 11 Polarization curves obtained from the alloy samples in SBF at 37 ℃. The inset is an enlarged view of the area highlighted in the dashed square showing the different current densities of the samples. The corrosion potential of aged samples decreases with ageing time, while the cathodic current density increases.

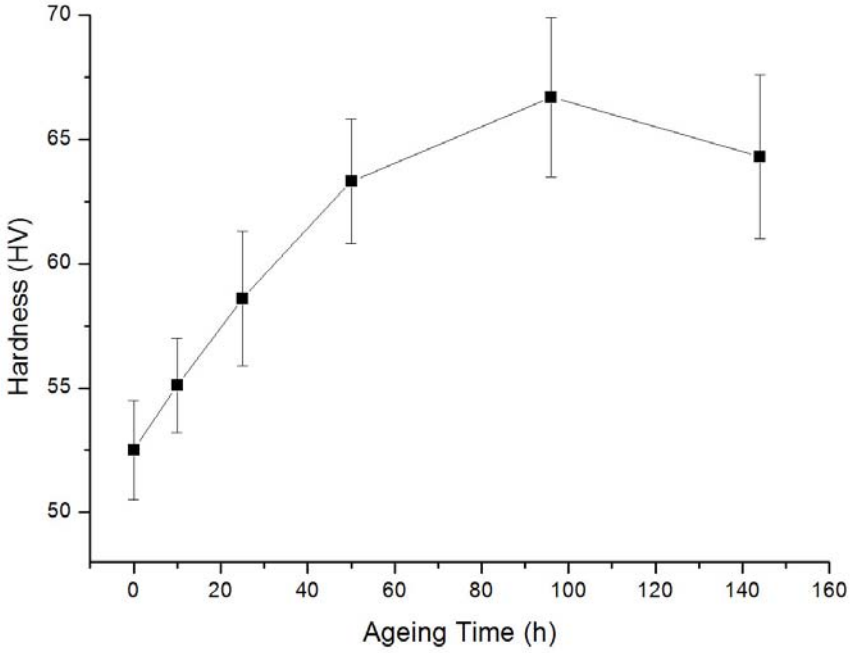

Figure 12 Hardness versus ageing time at 160 °C. The peak hardness is achieved at 96 h.

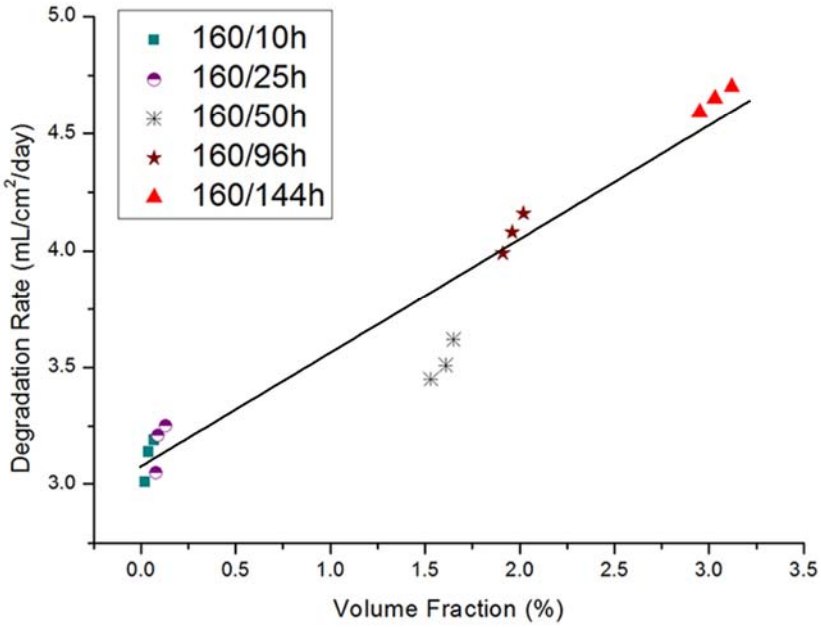

Figure 13 The relationship between the volume fraction of fine precipitates and the degradation rate in the aged samples.

Highlights

- Heat treatments (solution treatment and ageing) were used to change the microstructure and then their effects on the bio-corrosion rate of Mg-3Zn in simulated body fluid were studied.
- Nano-scale precipitates formed during ageing decrease the corrosion resistance.
- The increase in bio-corrosion rate with ageing time appears to be monotonic. With increasing ageing time, Mg alloys display worse corrosion resistance because of the precipitates.
- The corrosion morphology consists of parallel filament-like trenches which mirror the growth direction of the precipitates in the aged alloys.